Control-Oriented Modeling and Repetitive Control in In-Layer and Cross-Layer Thermal Interactions in Selective Laser Sintering

Dan Wang
Department of Mechanical Engineering,
University of Washington,
Seattle, WA 98195
e-mail: daw1230@uw.edu

Tianyu Jiang
Department of Mechanical Engineering,
University of Washington,
Seattle, WA 98195
e-mail: tjiang19@uw.edu

Xu Chen[1]
Department of Mechanical Engineering,
University of Washington,
Seattle, WA 98195
e-mail: chx@uw.edu

Although laser-based additive manufacturing (AM) has enabled unprecedented fabrication of complex parts directly from digital models, broader adoption of the technology remains challenged by insufficient reliability and in-process variations. In pursuit of assuring quality in the selective laser sintering (SLS) AM, this paper builds a modeling and control framework of the key thermodynamic interactions between the laser source and the materials to be processed. First, we develop a three-dimensional finite element simulation to understand the important features of the melt pool evolution for designing sensing and feedback algorithms. We explore how the temperature field is affected by hatch spacing and thermal properties that are temperature-dependent. Based on high-performance computer simulation and experimentation, we then validate the existence and effect of periodic disturbances induced by the repetitive in- and cross-layer thermomechanical interactions. From there, we identify the system model from the laser power to the melt pool width and build a repetitive control algorithm to greatly attenuate variations of the melt pool geometry. [DOI: 10.1115/1.4046367]

Keywords: adaptive control, control applications, digital/sampled data control, manufacturing systems

1 Introduction

Different from conventional subtractive machining, additive manufacturing (AM, also called 3D printing) builds up a part from its digital model by adding together materials layer by layer. This paper studies laser-based AM technologies, with a focus on the selective laser sintering (SLS) subcategory. This AM technology applies laser beams as the energy source to melt and join powder materials. A typical workpiece is built from many thousands of thin layers. Within each layer, the laser beam is controlled to follow trajectories predefined by the part geometry in a slicing process. After the sintering of one layer is finished, a new thin layer of powder is spread on top and then another cycle begins. SLS accommodates a broad range of materials (e.g., metals, polymers, and ceramics) and can build customized parts with complex features and high accuracy requirements. Despite the advantages and continuously emerging applications, broader adoption of the technology remains challenged by insufficient reliability and in-process variations. These variations are induced by, for example, environmental vibrations, powder recycling, imperfect laser-material interactions, and mechanical wears [1–3]. Predictive modeling and process control have thus been key for mitigating the variations and enhancing the energy deposition in SLS.

Several existing strategies employ numerical and control-oriented modeling to understand SLS and other laser-based AM processes such as laser metal deposition. In numerical modeling, most researchers adopt finite element analysis (FEA) to investigate thermal fields of the powder bed and substrate, melt pool geometries, and mechanical properties of the printed parts in the response of various scanning patterns, scan speeds, number of lasers, and overhanging structures [4–6]. In control-oriented modeling, current researches often implement low-order system models obtained from system identification techniques, taking laser power or scan speed as the input and melt pool temperature or geometry as the output [2,7–9]. Furthermore, [8,10] connect a nonlinear memoryless submodel in series with the linear system model to account for nonlinearities. [9] builds a spatial-domain Hammerstein model to identify the coupled repetitive in- and cross-layer dynamics. The Rosenthal equations give the analytical solutions for a moving laser source in thick and thin plates and have been used to predict the temperature distribution of the powder bed [11–14].

Based on the reduced-order models, existing researches [2,15,16] apply PID control to regulate the process parameters and reduce the in-process errors. From there, [17] adds a feedforward path for tracking improvement. Other controllers have also been shown capable in improving the dimensional accuracy of the printed parts, including but not limited to the sliding mode controller [10], predictive controller [7], and iterative learning controller [18]. Note that except for Ref. [2], which was developed for SLS, all the other reviewed controllers were tailored for laser metal deposition.

Stepping beyond current architectures, this study builds a modeling and control framework that accounts for FEA, control-oriented modeling, and advanced control strategies in a unified scheme. Focusing on the root cause and characteristics of imperfect laser-material interactions, we first develop a three-dimensional finite element simulation to characterize the melt pool evolution for designing sensing and feedback algorithms. We explore how the temperature field is affected by hatch spacing and thermal properties that are temperature-dependent. Along the course of framing the FEA and experimenting on an in-house built SLS testbed, we identify highly periodic melt-pool-width variations rising from the repetitive in- and cross-layer thermomechanical interactions. Then, we introduce repetitive control (RC) to attenuate these periodic variations that challenge conventional PID control. After identifying the system model from the laser power to the melt pool width, we build a plug-in RC algorithm and validate that its disturbance-attenuation performance is superior to that of PID control.

The remainder of this paper is structured as follows. Section 2 reviews a plug-in RC design. Section 3 builds and refines a

[1]Corresponding author.
Manuscript received October 23, 2019; final manuscript received February 7, 2020; published online February 14, 2020. Assoc. Editor: Reza Tafreshi.

numerical model of the SLS process. Section 4 verifies the existence of the periodic disturbances induced by the repetitive in- and cross-layer thermomechanical interactions. An RC algorithm is built in Sec. 5 to attenuate these periodic disturbances. Section 6 concludes the paper.

2 Preliminaries of Repetitive Control

RC is designed to track/reject periodic exogenous references/disturbances in applications with repetitive tasks [19]. By learning from previous iterations, RC can extensively enhance current control performance in the structured task space. In digital RC, an internal model $1/(1-z^{-N})$ is incorporated in the controller, where z is the complex indeterminate in the z-transform. N is the period of the signal and equals the sampling frequency (denoted in this paper as $1/T_s$ or f_s) divided by the fundamental disturbance frequency (f_0).

Consider a baseline feedback system composed of the plant $P(z)$ and the baseline controller $C(z)$ (Fig. 1 with the dotted box removed). $C(z)$ can be designed by common servo algorithms, such as PID, H_∞, and lead-lag compensation. The signals $r(k)$, $e(k)$, $d(k)$, and $y(k)$ represent, respectively, the reference, the tracking error, the input disturbance, and the system output. The sensitivity function $S(z)=1/(1+P(z)C(z))$ is the transfer function from $d(k)$ to $y(k)$.

This section introduces a plug-in RC design [20] that utilizes the internal signals $e(k)$ and $u(k)$ to generate a compensation signal $w(k)$ (Fig. 1). Let m denote the relative degree of $\hat{P}(z)$, the nominal model of $P(z)$. The transfer function of the overall controller from $e(k)$ to $u(k)$ is

$$C_{all}(z)=\frac{C(z)+z^{-m}\hat{P}^{-1}(z)Q(z)}{1-z^{-m}Q(z)} \tag{1}$$

The internal model is integrated in C_{all} if the Q filter is designed as $Q(z)=(1-\alpha^N)z^{m-N}/(1-\alpha^N z^{-N})$, that is, $1-z^{-m}Q(z)=(1-z^{-N})/(1-\alpha^N z^{-N})$, where $\alpha\in[0,\ 1)$ is a tuning factor that determines the attenuation width of $1-z^{-m}Q(z)$. Then at the harmonic frequencies $\omega_k=k2\pi f_0 T_s$ ($k\in\mathbb{Z}^+$, the set of positive integers), the magnitude responses of $1-z^{-m}Q(z)$ are zero because $1-e^{-j\omega_k N}=1-e^{-jk2\pi f_0 T_s/(f_0 T_s)}=1-e^{-jk2\pi}=0$. Hence, we have $|C_{all}(z)|\to\infty$ and the new sensitivity function $S_0(z)=1/(1+P(z)C_{all}(z))\approx(1-z^{-m}Q(z))/(1+P(z)C(z))=0$ with $z=e^{j\omega_k}$. At the intermediate frequencies $\omega\neq k2\pi f_0 T_s$, $Q(e^{j\omega})\approx 0$, and $|1-z^{-m}Q(z)|_{z=e^{j\omega}}\approx 1$ when α is close to 1; thus, $C_{all}(z)\approx C(z)$, and the original loop shape is maintained. A smaller α can yield a wider attenuation width at the cost of deviating from the baseline loop shape, as shown in Fig. 2.

During implementation, zero-phase pairs $q_0(z^{-1})q_0(z)$ are multiplied into $Q(z)$ for robustness against plant uncertainties at high-frequency regions:

$$Q(z)=\frac{(1-\alpha^N)z^{(m-N)}}{1-\alpha^N z^{-N}}q_0(z^{-1})q_0(z) \tag{2}$$

where $q_0(z)=(1+z)^{n_0}/2^{n_0}$ and $n_0\in\mathbb{Z}^+$ is the number of the zero-phase pairs (Fig. 3).

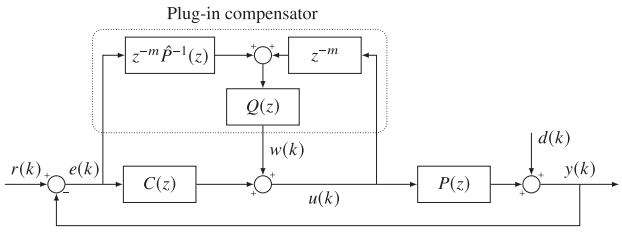

Fig. 1 Block diagram of a plug-in RC design

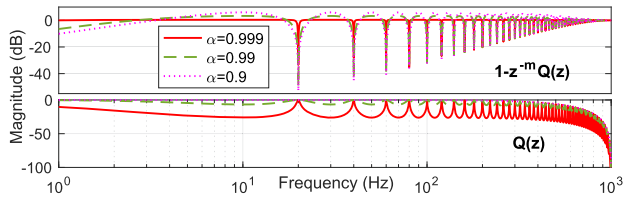

Fig. 2 Magnitude responses of $1-z^{-m}Q(z)$ and $Q(z)$ with different values of α and $n_0=1$ in the example of Sec. 5

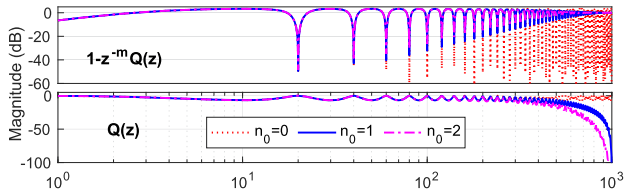

Fig. 3 Magnitude responses of $1-z^{-m}Q(z)$ and $Q(z)$ with different n_0 and $\alpha=0.99$ in the example of Sec. 5

3 Numerical Modeling in Selective Laser Sintering

We use the COMSOL Multiphysics 5.3a software to build and refine a finite element model for simulating the in- and cross-layer thermal cycles in SLS. The simulation considers surface convection, surface radiation, and conduction, while the effects of fluid flow and Marangoni force are neglected. We have also evaluated the effect of phase change, which is out of the scope of this paper and is omitted here.

3.1 Finite Element Analysis. The governing equation for the conduction heat flow in SLS is $\rho c_p(dT(x,\ y,\ z,\ t)/dt)=\nabla\cdot(k\nabla T(x,\ y,\ z,\ t))+q_s$, where k is the thermal conductivity, c_p is the specific heat, ρ is the effective density, t is the time, T is the temperature, and q_s is the rate of local internal energy generated per unit volume [11]. $T(x,\ y,\ z,\ t)$ is abbreviated to T in the following derivation. The process parameters used in the simulation are listed in Table 1 unless otherwise specified. Specially, the thermal properties k, c_p, and ρ are temperature-dependent (Fig. 4).

The initial condition is $T(x,\ y,\ z,\ 0)=T_0$, where T_0 is the initial temperature. Since it is assumed that the bottom has no heat loss, one boundary condition is $-k(\partial T/\partial z)|_{z=h}=0$, where h indicates the location of the bottom surface of the substrate. Considering surface conduction, convection, and radiation, the other boundary condition is $-k(\partial T/\partial z)|_{z=0}=-Q+h_c(T-T_e)+\varepsilon\sigma_B(T^4-T_e^4)$, where h_c is the convection heat transfer coefficient, T_e is the ambient temperature, ε is the emissivity, σ_B is the Stefan–Boltzmann constant, and Q is the input heat flux. Here, we assume Q has a Gaussian laser beam profile: $Q\approx(2P/\pi R^2)e^{-2r^2(x,y,z,t)/R^2}$, where P is the laser power, R is the effective laser beam radius, and r is the radial distance from the center of the laser spot.

The built model of a thin layer of powder bed and the substrate is depicted in Fig. 5. In this model, we use a selective mesh scheme to

Table 1 Parameters for numerical simulation

Parameters	Value	Parameters	Value
Powder bed size	15 mm × 15 mm × 50 μm	Material	Ti6Al4V
Substrate size	15 mm × 15 mm × 5 mm	Track length L	5 mm
R	220 μm/2	Time-step T_s	0.5 ms
Absorptance	0.25	Emissivity	0.35
T_{sol}	1873 K	Scan speed u_x	100 mm/s
L_f	295 kJ/kg	Laser power P	60 W
T_0/T_m	293.15 K/1923.15 K	ϕ_0	0.4
h_c	12.7 W/(m^2 K)	k, c_p, and ρ	See Fig. 4

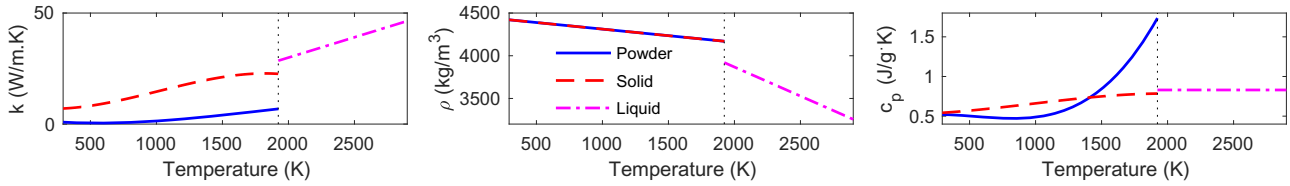

Fig. 4 Temperature-dependent thermal properties of Ti6Al4V [21]. The vertical dotted line indicates the melting point.

balance model accuracy with computation time: a fine triangular-and-swept mesh with the maximum element size of 72.6 μm (33% of the laser diameter, i.e., 0.33d) is applied to the central powder bed region that directly interacts with the energy beam, whereas less finer triangular-and-swept mesh (3.5 mm) and tetrahedral mesh (2 mm) are applied to the substrate and peripheral powder bed, respectively. We apply a bidirectional scan scheme, as illustrated in Fig. 5.

3.2 Mesh Refinement. In FEA, a correct model will move toward the exact solution as the mesh size decreases toward zero. To ensure the property of the built model, we conduct a mesh refinement study, as shown in Fig. 6. The horizontal axis denotes the element size that equals the laser diameter d divided by n. With n increasing, the mesh gets finer. We design 16 simulations with different element sizes ranging from $n=0.5$ (coarser) to $n=8$ (finer). Each simulation computes one sintering track of length 5 mm located in the middle of the powder bed. At the end of each simulation, the peak temperature of the melt pool already reaches the steady-state value. We then compare each steady-state value with that of the finest simulation ($n=8$), and the difference is plotted in the vertical axis of Fig. 6. As we can see, beyond $n=3$, the peak temperature starts converging to the exact solution, and the benefit of keeping reducing the element size becomes insignificant. Throughout this paper, we select 0.33d as the element size of the central power bed where lie the laser tracks.

3.3 Hatch Spacing. Implementing the developed finite element model, we will examine next how hatch spacing affects the melt pool variation especially during the transition from the end point of one track (named P1) to the start point of the adjacent track to be sintered (P2). Here, hatch spacing is defined as the distance between two adjacent laser tracks.

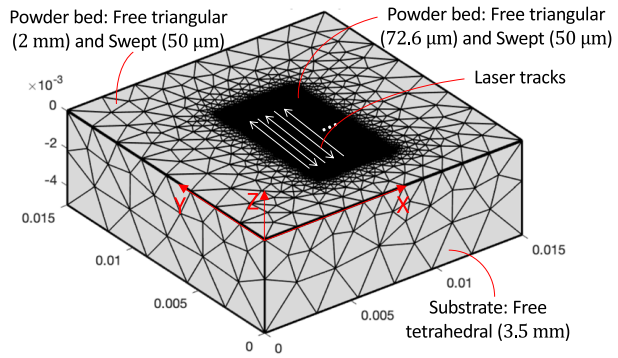

Fig. 5 Selective meshing and in-layer laser sintering

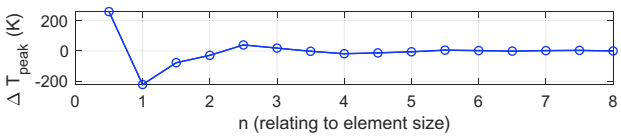

Fig. 6 Mesh refinement. Element size=laser diameter/n.

When the hatch spacing (e.g., 47 μm in (a1)–(a4) of Fig. 7) is much less than half of the melt pool width (around the laser spot radius 110 μm), the laser spot at P2 will be centered inside the melt pool region of P1 and thus can take advantage of the accumulated heat, yielding a well-developed melt pool at $t=0.0505$ s. Otherwise, when the hatch spacing (e.g., 100 μm in (b1)–(b4) of Fig. 7) is close to or larger than half of the melt pool width, the laser spot at P2 will be centered out of the melt pool region of P1, yielding a lower initial temperature at P2. Thus, the melt pool evolves slower, and two immature states show up at $t=0.5505$ s and $t=0.551$ s.

In SLS, to get a consistent part quality, a stable melt pool is desired during the transition. The immature melt pool states can be eliminated by decreasing the hatch spacing. However, there is a trade-off between melt pool stability and sintering efficiency since simply shortening the hatch spacing increases printing time.

4 Periodic Thermal Interaction in Selective Laser Sintering

This section employs the developed finite element simulation and the experimentation in an in-house built SLS machine to validate the existence of periodic disturbances in SLS. These periodic disturbances come from the repetitive in- and cross-layer thermomechanical interactions, as will be investigated in Secs. 4.1 and 4.2, individually. The combined thermal effect will be elaborated in Sec. 4.3.

4.1 In-Layer Numerical Modeling. Using the finite element model developed in Sec. 3, 80 tracks are bidirectionally sintered within one layer (Fig. 5). From the simulation results in Fig. 8(a), we observe that the melt pool width fluctuates around the average value 216 μm (close to the laser spot diameter 220 μm) after reaching the steady-state. Most importantly, the start of each track has larger melt pool widths than the rest of the track. This is because in bidirectional scanning, when the energy beam approaches the end of one track, the large latent heat does not have enough time to dissipate out before the next track starts. The resulting increased

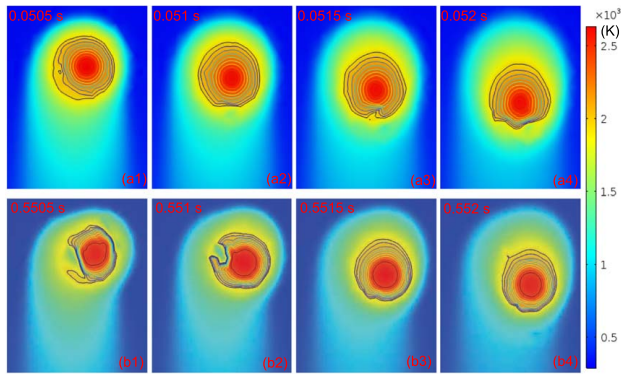

Fig. 7 Melt pool variation at the start of the second track with hatch spacing of 47 μm in (a1)–(a4) and the start of the 12th track with hatch spacing of 100 μm in (b1)–(b4)

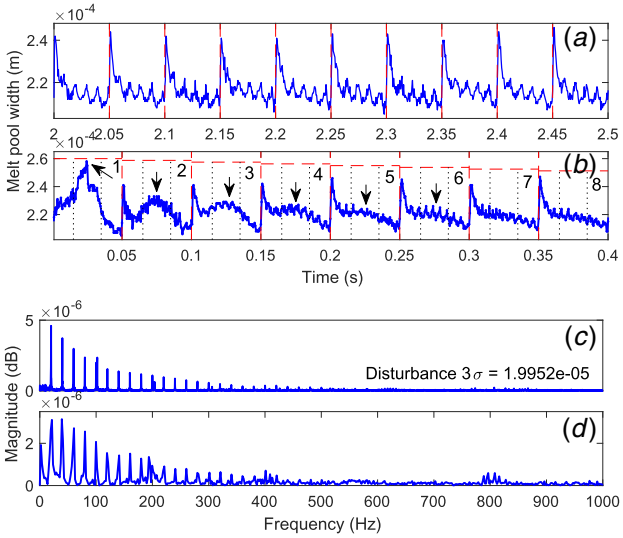

Fig. 8 Evolution of melt pool width. In-layer thermal interaction in (*a*) time domain and in (c) Fast Fourier transform (FFT). Combined in- and cross-layer thermal interaction in (*b*) time domain and in (*d*) FFT.

melt pool widths at the beginning of each track form a periodic disturbance with a repetitive spectrum in the frequency domain (Fig. 8(*c*)).

Note that besides the bidirectional scan used here, other scan patterns yield similar repetitive disturbances (see, e.g., experimental results in Ref. [22]). Here, automatic control algorithms [1,20] can be brought in to handle those undesired repetitive spectra, as will be discussed in Sec. 5.

4.2 Cross-Layer Experimental Verification. Similar to the in-layer case where previously sintered tracks generate thermal disturbances to the new track, the heating-cooling cycles of previously sintered layers also create disturbances to the temperature profile of the top layer. This cross-layer thermal disturbance is particularly harmful to parts with abrupt geometric changes, such as overhang structures. We verify in this section the existence of the cross-layer thermal patterns based on the experimental results collected from an in-house built SLS testbed (Fig. 9).

In the experimental setup, an aluminum part is buried in the Nylon 12 powder bed and directly attached to the build plate that is heated by heat resistors from underneath. A few thin layers of the powder are spread on top of the flat rectangular surface of the part. At the stage of pre-heating, since aluminum has a higher thermal conductivity than Nylon 12, the temperature of the powders on top of the part surface is significantly higher than that of the powders elsewhere (top plots in Fig. 9). The surface thermal profile of the powder bed is recorded by a FLIR A325sc infrared camera. A 2.8-Watt 445 nm laser diode that gives the desired energy density is used to fuse the powder materials bidirectionally. Also, the laser scan pattern has a larger length than the aluminum part sitting below. This configuration imitates the sintering process of parts with overhang structures, where the aluminum part corresponds to the previously fused layers. Note that we intentionally select a large hatch spacing of 10 mm such that the in-layer thermal interaction is negligible.

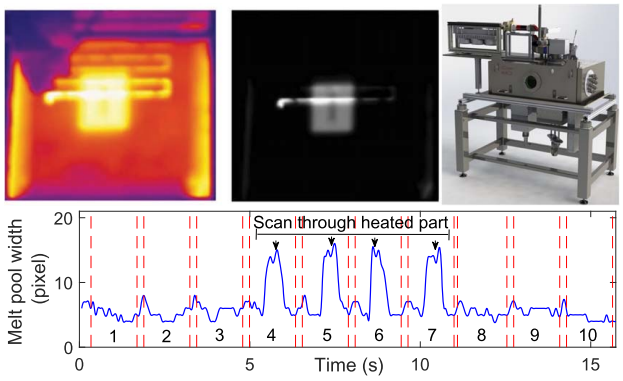

Fig. 9 Illustration of cross-layer disturbance. Top left: thermal image during sintering. Top middle: processed image in gray-scale. Top right: in-house built SLS testbed. Bottom: temporal evolution of melt pool width showing cross-layer thermal interaction.

From the bottom plot in Fig. 9, we recognize significant repetitive variations of the melt pool width (evaluated by pixel numbers in the video frames). When the laser scans through the powder right on top of the aluminum part, larger melt pool widths are detected due to higher initial temperatures of the powders therein (Tracks 4–7).

4.3 In- and Cross-Layer Numerical Modeling. This section employs the developed finite element model in Sec. 3 to demonstrate the combined effect of periodic in- and cross-layer thermal interactions. We put under the powder bed a Ti6Al4V part ($4.45 \times 1 \times 1$ mm^3) that is preheated to 1200 K. Due to the high initial temperature of the added part, the powder on top of the part has a higher initial temperature than the powder elsewhere. We also use the selective mesh scheme here: triangular-and-swept (72.6 μm) for the central powder bed, triangular-and-swept (1.5 mm) for the peripheral powder bed, and free tetrahedra (2 mm) for the substrate and the added part. The scan strategy is the same as that in Fig. 5. Eight tracks are sintered bidirectionally with the hatch spacing of 50 μm. The length of the laser track (5 mm) is greater than that of the added part (1 mm). This configuration similar to that in Sec. 4.2 simulates the sintering of the overhang structure.

Figure 10 illustrates the top views of the surface temperature profiles during the first-track sintering from 0 to 0.05 s. When the laser is passing through the preheated powder at 0.025 s, we get a larger melt pool width, compared to when the laser is approaching ($t =$ 0.0135 s) or leaving ($t = 0.05$ s) the preheated region. The larger melt pool width is due to the higher initial temperature of powder on top of the preheated part. This result coincides with that in Sec. 4.2. Moreover, as time goes by, the temperature difference between the preheated part and the ambient material is getting smaller, as shown by the blurrier border of the preheated region at $t = 0.05$ s in Fig. 10.

During the evolution of the melt pool width in Fig. 8(*b*), at the beginning of each track, there is a large increase of the melt pool width caused by the in-layer thermal interaction, as explained in Sec. 4.1. Furthermore, we can tell from the arrowed peaks between two adjacent dotted lines that larger melt pool widths will be created every time the laser scans through the powder on top of the preheated part (corresponding to previously fused layers). Also, these peaks caused by the cross-layer thermal interaction get smaller as the heat accumulated by the preheated part

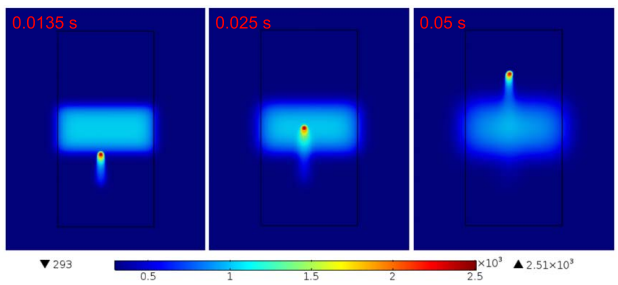

Fig. 10 Surface temperature distributions in K (top view) during sintering the first track

dissipates out (Tracks 7 and 8 in Fig. 8(*b*)). Compared with the bottom plot in Fig. 9, the amplitudes of these peaks fall faster because Ti6Al4V has a larger thermal conductivity than Nylon 12.

In summary, we have demonstrated that the periodic evolution of the melt pool width is a lumped output of the repetitive in- and cross-layer heat transfer dynamics. When comparing the frequency spectra in Figs. 8(*c*) and 8(*d*), we can tell that the cross-layer variations change the magnitudes of the spectral peaks but not the main harmonic frequency values. These major repetitive variations can thus be attenuated by the same feedback control algorithms. As a case study, we implement the plug-in RC presented in Sec. 2 to reduce the periodic disturbances caused by the repetitive in-layer thermomechanical interaction.

5 Repetitive Control in Selective Laser Sintering

In this section, we first employ a pseudorandom binary sequence (with a magnitude of 10 W and an add-on DC component of 60 W) as the input signal to identify the plant model between the laser power and the melt pool width: $P(s) = 0.0009013/(s + 945.8)$.

As shown in Fig. 11, the frequency responses of the measured and identified systems match well with each other. We thereupon design a PI controller as $C(s) = K_p + K_i/s$ with $K_p = 1.56 \times 10^6$ and $K_i = 2.48 \times 10^9$. Under the sampling time T_s of 0.5 ms (i.e., $f_s =$ 2 kHz), the zero-order-hold equivalents of the plant and controller models, respectively, are $P(z) = (3.591 \times 10^{-7})/(z - 0.6232)$ and $C(z) = (1.56 \times 10^6 z - 3.2 \times 10^5)/(z - 1)$.

The solid line in the top plot of Fig. 12 shows the magnitude response of the sensitivity function $S(z)$ in the baseline feedback loop composed of $P(z)$ and $C(z)$. Such a design provides a bandwidth at 184 Hz, which approximates the limit of 20% of the Nyquist frequency (1000 Hz) and indicates that the controller is well tuned.

In the in-layer sintering, a periodic disturbance existing in the evolution of the melt pool width is induced by the repetitive thermal interaction between current track and previous tracks (Sec. 4.1). The repetitive spectrum of this disturbance in the frequency domain is exhibited in Fig. 8(*c*). The fundamental frequency f_0 of the disturbance is determined by the duration of scanning one track t_0, that is, $f_0 = 1/t_0 = u_x/L$, where u_x is the scan speed and L is the track length. In this example, $f_0 = 100/5 = 20$ Hz and frequency spikes at nf_0 ($n \in \mathbb{Z}^+$) appear in the fast Fourier transform (FFT) of the disturbance. We first build the baseline feedback loop consisting of $P(z)$ and $C(z)$ to attenuate the disturbance. From Fig. 13, we have

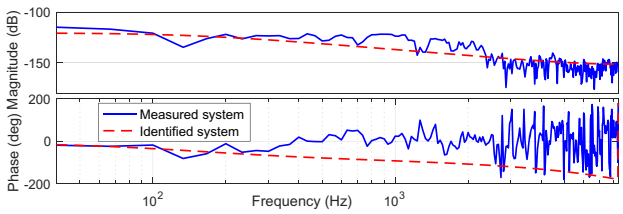

Fig. 11 Measured and identified system responses

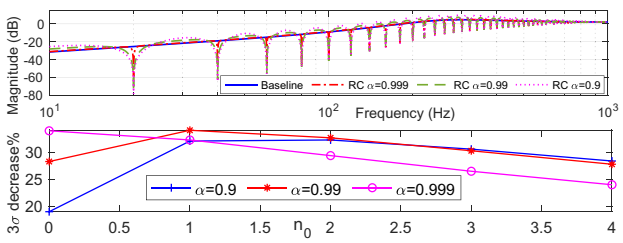

Fig. 12 Top: magnitude responses of sensitivity functions $S(z)$ in baseline control and $S_0(z)$ in RC with different values of α and $n_0 = 1$. Bottom: 3σ decreases with varying α and n_0.

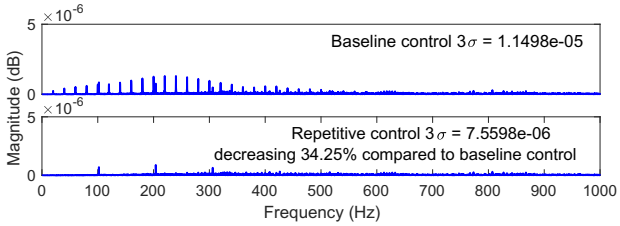

Fig. 13 FFT of plant outputs ($y(k)$ in Fig. 1) with baseline control and RC ($\alpha = 0.99$ and $n_0 = 1$)

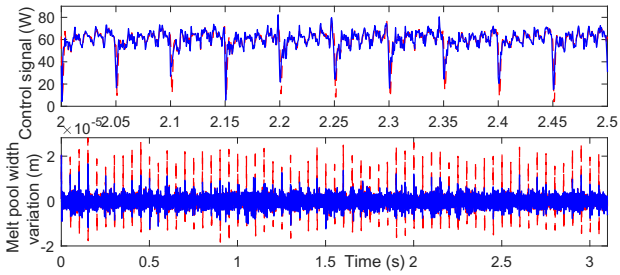

Fig. 14 Top plot: control signals ($u(k)$ in Fig. 1) of baseline control (dashed) and RC (solid). Bottom plot: melt pool width variations ($y(k)$ in Fig. 1) of baseline control (dashed) and RC (solid).

that the baseline PI control can attenuate to some extent the frequency spikes below the closed-loop bandwidth (184 Hz) but leave the other high-frequency spikes untouched. To enhance the disturbance-attenuation performance, the plug-in RC compensator introduced in Sec. 2 is added on top of the baseline controller.

In the design of the Q filter in Eq. (2), the relative degree m of $\hat{P}(z)$ is 1, and the disturbance period $N = f_s/f_0 = 2000/20 = 100$. High-gain control efforts are generated exactly at 20 Hz and its harmonics (see $S_0(z)$ in the top plot of Fig. 12). We then search around to find the optimal pair of α and n_0 that gives the best disturbance-attenuation result. With α decreasing, the decreasing spikes of $1 - z^{-m}Q(z)$ and $S_0(z)$ at harmonic frequencies get wider and deeper, but the intermediate frequency spikes are amplified (Fig. 2 and top plot of Fig. 12). With n_0 increasing, frequency spikes at high frequencies are further attenuated at the cost of shallower decreasing spikes at the harmonics (Fig. 3). To balance between attenuations at the harmonics and amplifications elsewhere, we plot in Fig. 12 the decrease of the 3σ value of the output ($y(k)$ in Fig. 1) with varying values of α and n_0, where σ denotes the standard deviation. With the plug-in RC added to the baseline PI control, the more the 3σ value decreases, the further the disturbance is attenuated. Based on the bottom plot of Fig. 12, we choose the pair of $\alpha = 0.99$ and $n_0 = 1$ that has the maximum 3σ decrease. Substituting the values of m, N, α, and n_0 into (2), we thus get the transfer function of the Q filter.

The feedback loop with the plug-in RC compensator is designed according to Fig. 1 with $r(k) = 0$ and $d(k)$ coming from the cross-scan thermodynamics interaction (Fig. 8(*a*) with the mean removed). The control signals $u(k)$ of the baseline control and RC are shown in the top plot in Fig. 14. We can tell from Fig. 13 that compared with the baseline control, the application of RC further lowers the periodic frequency spikes especially at high frequencies beyond the closed-loop bandwidth and decreases the 3σ value by 34.25%. Similarly, in the time domain, the increased control efforts of RC at the harmonic frequencies yield a further-attenuated output $y(k)$ (bottom plot in Fig. 14).

6 Conclusion

In this paper, we first developed a finite element model to simulate the temperature response of the repetitive energy deposition in

SLS. We briefly discussed the effect of hatch spacing on the property of the model. Employing high-performance computation and experimentation, we validated the existence of the periodic disturbances in the evolution of melt pool width. The disturbance periodicity is closely related to the recurring laser scanning trajectories and the repetitive in- and cross-layer thermomechanical interactions. From there, we identified the system model from the laser power to the melt pool width and built a repetitive control algorithm to advance the part quality in SLS. We validated that the repetitive control algorithm attenuates the periodic disturbances more substantially compared to the PI control.

Acknowledgment

This material is based upon work supported in part by the National Science Foundation under Grant No. 1953155.

References

[1] Wang, D., and Chen, X., 2018, "A Multirate Fractional-Order Repetitive Control for Laser-Based Additive Manufacturing," Control Eng. Pract., **77**, pp. 41–51.
[2] Kruth, J.-P., Mercelis, P., Van Vaerenbergh, J., and Craeghs, T., 2007, "Feedback Control of Selective Laser Melting," Proceedings of the 3rd International Conference on Advanced Research in Virtual and Rapid Prototyping, Leiria, Portugal, Sept. 24–29, pp. 521–527.
[3] Seyda, V., Kaufmann, N., and Emmelmann, C., 2012, "Investigation of Aging Processes of ti-6al-4 V Powder Material in Laser Melting," Phys. Proc., **39**, pp. 425–431.
[4] Masoomi, M., Thompson, S. M., and Shamsaei, N., 2017, "Laser Powder Bed Fusion of ti-6al-4v Parts: Thermal Modeling and Mechanical Implications," Int. J. Mach. Tools Manuf., **118**, pp. 73–90.
[5] Hussein, A., Hao, L., Yan, C., and Everson, R., 2013, "Finite Element Simulation of the Temperature and Stress Fields in Single Layers Built Without-Support in Selective Laser Melting," Mater. Des. (1980–2015), **52**, pp. 638–647.
[6] Foroozmehr, A., Badrossamay, M., Foroozmehr, E., and Golabi, S., 2016, "Finite Element Simulation of Selective Laser Melting Process Considering Optical Penetration Depth of Laser in Powder Bed," Mater. Des., **89**, pp. 255–263.
[7] Song, L., and Mazumder, J., 2011, "Feedback Control of Melt Pool Temperature During Laser Cladding Process," IEEE Trans. Control Syst. Technol., **19**(6), pp. 1349–1356.
[8] Cao, X., and Ayalew, B., 2015, "Control-Oriented Mimo Modeling of Laser-Aided Powder Deposition Processes," American Control Conference (ACC), Chicago, IL, July 1–3, IEEE, pp. 3637–3642.
[9] Sammons, P. M., Bristow, D. A., and Landers, R. G., 2014, "Repetitive Process Control of Laser Metal Deposition," ASME 2014 Dynamic Systems and Control Conference, American Society of Mechanical Engineers, ASME, p. V002T35A004.
[10] Fathi, A., Khajepour, A., Durali, M., and Toyserkani, E., 2008, "Geometry Control of the Deposited Layer in a Nonplanar Laser Cladding Process Using a Variable Structure Controller," ASME J. Manuf. Sci. Eng., **130**(3), p. 031003.
[11] Kannatey-Asibu, E., Jr., 2009, *Principles of Laser Materials Processing*, Vol. 4, John Wiley & Sons, Hoboken, NJ.
[12] Tang, M., Pistorius, P. C., and Beuth, J. L., 2017, "Prediction of Lack-of-Fusion Porosity for Powder Bed Fusion," Addit. Manuf., **14**, pp. 39–48.
[13] Mirkoohi, E., Ning, J., Bocchini, P., Fergani, O., Chiang, K.-N., and Liang, S., 2018, "Thermal Modeling of Temperature Distribution in Metal Additive Manufacturing Considering Effects of Build Layers, Latent Heat, and Temperature-Sensitivity of Material Properties," J. Manuf. Mater. Proc., **2**(3), p. 63.
[14] Li, J., Wang, Q., Michaleris, P. P., Reutzel, E. W., and Nassar, A. R., 2017, "An Extended Lumped-Parameter Model of Melt–Pool Geometry to Predict Part Height for Directed Energy Deposition," ASME J. Manuf. Sci. Eng., **139**(9), p. 091016.
[15] Hofman, J., Pathiraj, B., Van Dijk, J., de Lange, D., and Meijer, J., 2012, "A Camera Based Feedback Control Strategy for the Laser Cladding Process," J. Mater. Process. Technol., **212**(11), pp. 2455–2462.
[16] Salehi, D., and Brandt, M., 2006, "Melt Pool Temperature Control Using Labview in Nd: Yag Laser Blown Powder Cladding Process," Int. J. Adv. Manuf. Technol., **29**(3), pp. 273–278.
[17] Fathi, A., Khajepour, A., Toyserkani, E., and Durali, M., 2007, "Clad Height Control in Laser Solid Freeform Fabrication Using a Feedforward Pid Controller," Int. J. Adv. Manuf. Technol., **35**(3), pp. 280–292.
[18] Tang, L., and Landers, R. G., 2011, "Layer-to-Layer Height Control for Laser Metal Deposition Process," ASME J. Manuf. Sci. Eng., **133**(2), p. 021009.
[19] Inoue, T., Nakano, M., Kubo, T., Matsumoto, S., and Baba, H., 1981, "High Accuracy Control of a Proton Synchrotron Magnet Power Supply," IFAC Proc. Vol., **14**(2), pp. 3137–3142.
[20] Chen, X., and Tomizuka, M., 2014, "New Repetitive Control with Improved Steady-State Performance and Accelerated Transient," IEEE Trans. Control Syst. Technol., **22**(2), pp. 664–675.
[21] Arce, A. N., 2012, *Thermal Modeling and Simulation of Electron Beam Melting for Rapid Prototyping on Ti6Al4V Alloys*, North Carolina State University, Raleigh, NC.
[22] Dunbar, A. J., Denlinger, E. R., Gouge, M. F., Simpson, T. W., and Michaleris, P., 2017, "Comparisons of Laser Powder Bed Fusion Additive Manufacturing Builds Through Experimental in Situ Distortion and Temperature Measurements," Addit. Manuf., **15**, pp. 57–65.